Use of X-ray Computed Tomography for Understanding Localised, Along-the-Channel Degradation of Polymer Electrolyte Fuel Cells

Jennifer Hack[1], Lara Rasha[1], Patrick L. Cullen[3,1], Josh J. Bailey[1], Tobias P. Neville[1], Paul R. Shearing[1], Nigel P. Brandon[2], Dan J.L. Brett[1]*

[1]Electrochemical Innovation Lab, Department of Chemical Engineering, University College London, London, WC1E 7JE, UK

[2]Department of Earth Sciences and Engineering, Royal School of Mines, Imperial College London, London SW7 2BP, UK

[3]School of Engineering and Materials Science (SEMS) and Material Research Institute, Queen Mary University of London, London, E1 4NS, UK

* Author to whom correspondence should be addressed

Tel.: +44(0)20 7679 3310

Web: www.ucl.ac.uk/electrochemical-innovation-lab

Email: d.brett@ucl.ac.uk

1 Highlights

- Combined miniature fuel cell and X-ray computed tomography
- Identical-location X-ray CT along-the-channel of a serpentine flow field during accelerated stress testing
- Significant regional variation in the extent of degradation of the cathode
- Fuel cell carbon corrosion ASTs do not age electrodes homogeneously.

Abstract

The need to understand the effects of degradation in polymer electrolyte fuel cells (PEFCs) has led to the development of *in-situ* and *operando* imaging studies of failure

mechanisms occurring in their constituent materials, but studies using X-ray computed tomography (X-ray CT) for imaging have focussed primarily on a single region of the PEFC flow channel. Whilst studies have shown local variation in degradation rates using electrochemical techniques, this work employs identical-location X-ray CT imaging to elucidate the local degradation of a membrane electrode assembly (MEA) at various locations along-the-channel of a serpentine flow field. Using a carbon corrosion specific accelerated stress test (AST), in-depth analyses of the catalyst layers (CLs) and crack network allow for quantification of the material's degradation at the inlet, middle and outlet regions of the flow channel on the cathode side. Imaging of the regions was done after 0, 2000 and 5000 cycles and results show significant regional variation in the extent of degradation of the cathode CL. The order of degradation was found to be outlet > middle > inlet, with the outlet CL found to be thinner than the middle and inlet regions, with a greater extent of cracking. Furthermore, additional land and channel degradation effects were probed, with the land regions found to be less degraded than channel regions. This work further highlights the need to understand and develop ASTs that can promote a more uniform degradation rate across an MEA.

Graphical abstract

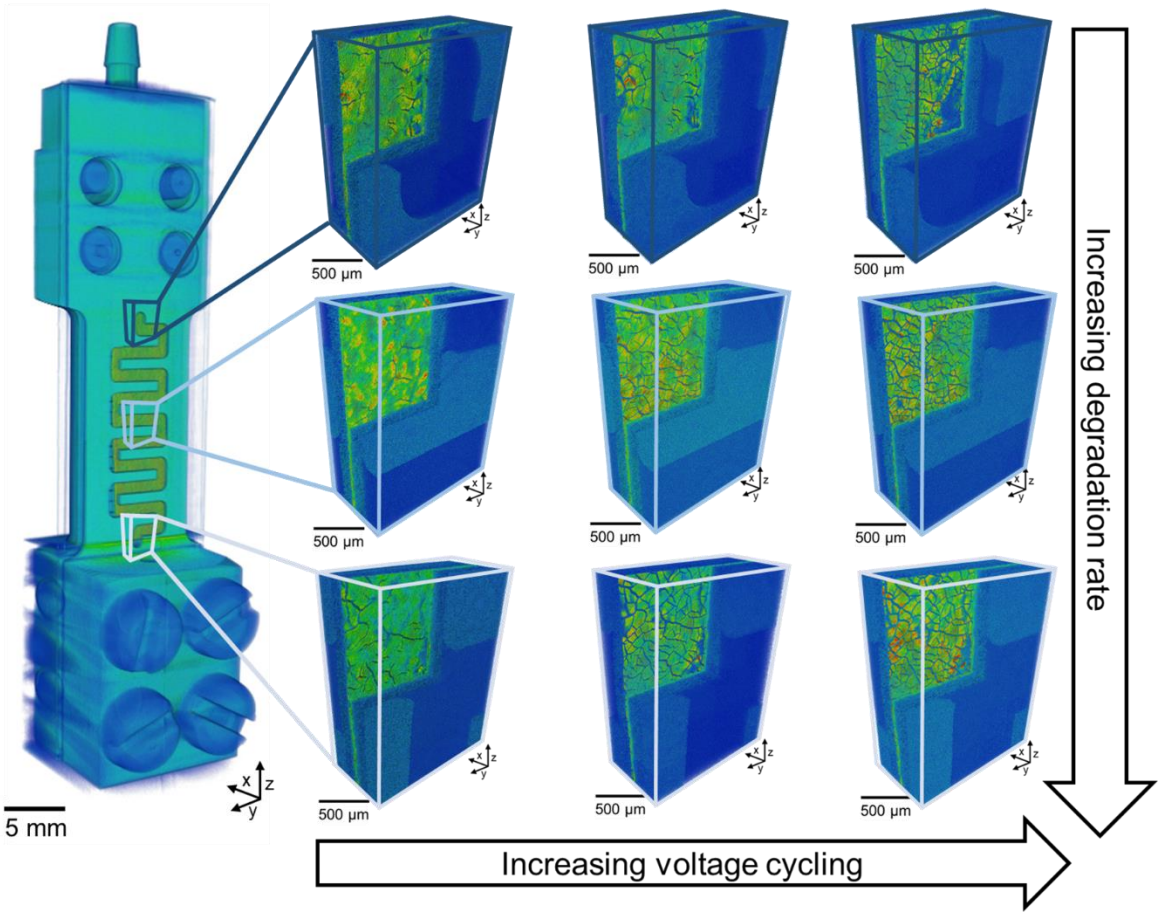

Keywords

Membrane electrode assembly; X-ray computed tomography; local degradation; polymer electrolyte fuel cell; accelerated stress test; carbon corrosion

2 Introduction

The urgent need for clean energy alternatives has seen a growth in the research, development and use of polymer electrolyte fuel cells (PEFCs) in applications ranging from transport [1] to stationary power [2]. As with many electrochemical technologies, issues concerning durability and lifetime of materials remain key challenges for improving the performance and lifetime. Accelerated stress tests (ASTs) are extensively used to antagonise and mimic degradation mechanisms within the PEFC on a timescale that is suitable for lab-based testing [3,4].

The ASTs are designed to target the degradation of different components of the membrane electrode assembly (MEA), from membrane failure to loss and degradation of catalyst and carbon support [5]. The carbon support is particularly prone to degradation at high overpotentials that occur during cell start-up/shut-down [6], from hydrogen/air fronts passing through the anode and cathode [7] and finally from changes in the MEA humidity [8]. There are several characteristic mechanisms carbon support degradation, which affect the electrode nano- and microstructure in a number of ways. Loss of carbon support material leads to compaction and collapse of the catalyst layer (CL), which leads to CL thinning [6,9]. Microstructural changes occur due to the formation and growth of cracks in the CL [10], which have been found to extend into the microporous layer (MPL) [11] and membrane [12]. Finally, the loss of carbon support also results in a loss of electrochemical surface area (ECSA), since platinum nanoparticles on the surface of the carbon are lost *via* detachment, dissolution or agglomeration [13]. A common assumption in the use of these ASTs is that the degradation process is occurring uniformly across the extent of the fuel cell, such that the imposed conditions are the determining factors and not the size of the cell or flow-field design. However, just as it is well established that fuel cell performance can be highly heterogeneous, so may the effects of the AST.

To better understand the internal workings and structural changes occurring during degradation testing, an increasing body of work is being reported on the design and operation of miniaturised PEFCs for use in *in-situ* and *operando* studies using X-ray computed tomography (X-ray CT), as discussed in the reviews of Meyer *et al.* [14] and Heenan *et al.* [15]. Such studies are carried out either on synchrotron beamlines at national facilities [16–18] or in laboratory-based X-ray CT instruments [19]. The design of an *in-situ* device is a trade-off between obtaining a reasonable (representative) fuel cell performance and creating a cell that is small enough in size to fit inside the instrument of choice and image features at the resolution of interest. Furthermore, the effect of the beam on the sample and performance of the cell must be considered and studies on synchrotron beamlines have shown that the X-ray intensity and dose will have an impact on fuel cell performance [20]. On the other hand, no appreciable deterioration of fuel cell performance was observed for testing in lab-based sources [21].

A large portion of *in-situ* and *operando* studies has been focussed on observation of water formation inside the MEA of the fuel cell. The MEA comprises two electrodes that sandwich a polymeric membrane. Each gas diffusion electrode (GDE) has a layered structure, consisting of the CL, the MPL and the gas diffusion layer (GDL). Observations of water in the pores of the MPL carried out by Alrwashdeh *et al.* [22] showed that an inhomogeneous distribution of droplets formed in the pores, with some being filled and some empty. Other work has included studies of water formation at the nano- and micro-scale [23], as well as the use of 3D printed flow-fields for visualising water [19] and sub-second imaging of water forming inside the pores of the GDL [24].

Fewer studies have been concerned with understanding the evolution of morphological changes inside the MEA as a result of ASTs. Work by Ramani *et al.* [25] and Singh [12,26] have shown how crack formation and evolution occurs in the membrane by carrying out simultaneous relative humidity (RH) cycling and imaging at the micron length scale. Crack formation has also been observed in the CL as a result of voltage cycling degradation tests [19,27], as reported by White *et al.* [10], where it was observed that cracks were found to widen over the course of the AST, which was accompanied by thinning of the CL.

Whilst these studies highlight the extent of degradation in one region of the MEA, they do not account for the varying rate of degradation along the length of a flow channel from the cathode gas inlet to cathode gas outlet. Some work has used electrochemical techniques to demonstrate this localised degradation, such as the recent work by Komini Babu *et al.*, which highlighted that the degradation of a PEFC during startup and shutdown cycles was non-uniform across the MEA. Using a specially designed segmented cathode, the localised electrochemical performance could be analysed and an inhomogeneous performance distribution was observed across the MEA from inlet to outlet over the course of degradation [28]. Other work by Garcia-Sanchez *et al.* has used current mapping to show the localised degradation of PEFCs, with SEM used for ex-situ visualisation of platinum in the membrane [29]. Such non-uniform degradation has been reported by a number of practitioners, but, until now, only in 2D, ex-situ SEM studies [11,28–30] or by using nano-scale techniques, like X-ray absorption fine structure (XAFS) or scanning transmission electron

microscopy-energy dispersive X-ray spectroscopy (STEM-EDS) [31]. However, 3D imaging of the microstructural degradation effects that accompany localised electrochemical degradation have not been demonstrated.

Considering this need to understand the “along-the-channel” morphological degradation of materials of the MEA, this work presents a combined 4D (3 spatial dimensions plus extent of voltage cycling in time) investigation into the localised degradation of the cathode CL during an AST. To the authors’ best knowledge, this is the first time that variation in MEA degradation along the flow channel of a serpentine flow field has been studied using X-ray CT.

3 Experimental and Methodology

3.1 Materials and electrochemical methods

A bespoke fuel cell was designed for *in-situ* imaging in a lab-based X-ray CT instrument (Figure 1a). Graphite plates, with diameter of 7.2 mm were used as flow-field, current collector and end plate, delivering gas to the MEA, *via* an etched serpentine flow-field, which includes both channel bends and adjacent channels to better mimic common flow-field designs found in larger cells. Current collection was done by attaching potentiostat load cables of a Gamry Interface 5000 (Gamry, USA) directly onto the fuel cell casing. The MEA was prepared by cutting two commercial gas diffusion electrodes (GDEs) (Hyplat, South Africa), with a platinum loading of 0.4 mg_{Pt} cm^{-2} on both the anode and cathode and an electrode area of 1.7 cm^2. The GDEs were hot-pressed onto a GORE-SELECT M8 30.25 membrane (Gore, USA) between two heated platens in a hot-press (Carver Inc., USA) at 150 °C for 3 minutes. The cell was assembled using nylon compression screws inserted *via* holes milled into the fuel cell casing, which ensured good alignment of the MEA with the flow fields, as well as providing electrical insulation between end plates. The MEA compression was 20%, which was calculated by comparing a) the MEA thickness prior to cell assembly measured with a micrometer with b) the MEA thickness measured using the X-ray CT dataset from the BOL Versa scans. The bottom set of screws fitted directly into a custom holder that could be mounted onto the stage of the Zeiss XRadia Versa 520

X-ray micro-CT instrument (Zeiss, USA), to ensure identical positioning of the sample in each scan and to reduce the risk of movement of the cell.

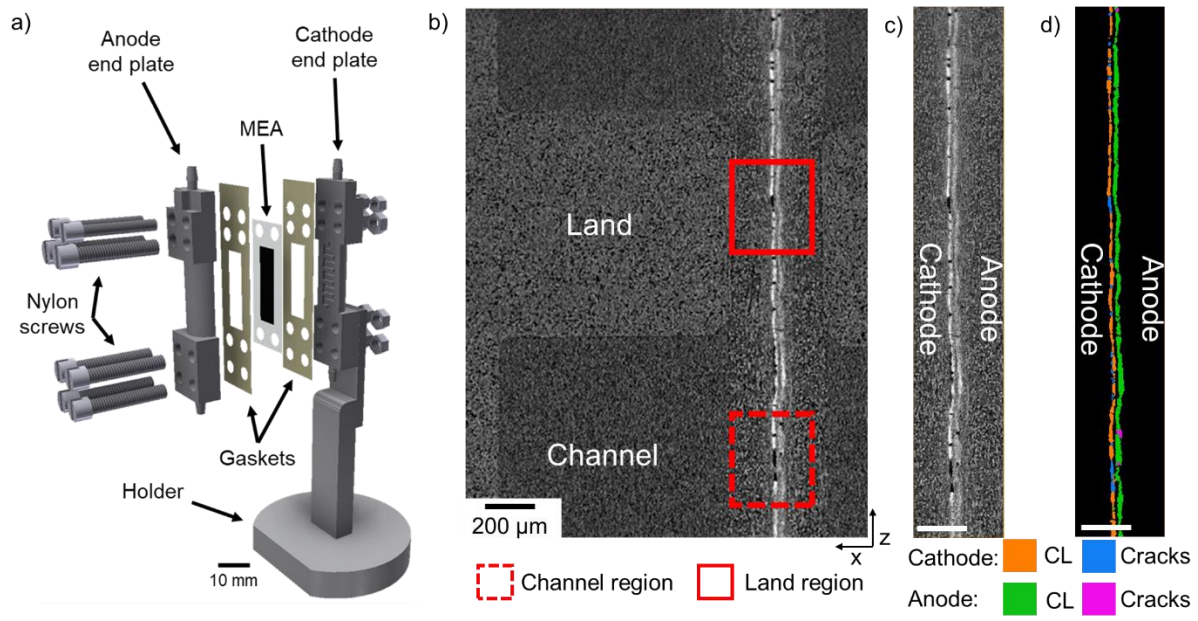

Figure 1 Exploded CAD view of the cell assembly, including graphite plates, gaskets and the MEA. Holes were milled for compression screws, which screw through the integrated holder; b) *xz* orthoslice of the middle region after 2000 cycles, showing the channel and land and indicating the regions that were extracted for channel (red dashed line) and land (red solid line) analyses; c) cropped grayscale orthoslice (middle, 2000 cycles) used for image segmentation and d) the segmented image, showing cathode CL (orange), cathode cracks (blue), anode CL (green) and anode cracks (pink). The white scalebar in c) and d) represents 200 µm and the axes coordinates are the same as those in b).

Gases were supplied at ambient pressure to the anode and cathode using Bronkhorst mass flow controllers (Bronkhorst, Netherlands) with a fixed flow of 20 mL min^{-1} and 100 mL min^{-1} on anode and cathode, respectively; this corresponds to a stoichiometry of 2:3 hydrogen:air at a current density of 1 A cm^{-2}. Humidification was provided by bubbling gas through de-ionised water before entering the cell. Tubing was insulated to avoid condensation on the walls of the piping and the cell was operated without additional heating. Polarisation curves were collected whilst flowing air over the cathode and the flow was changed to nitrogen for collection of cyclic voltammograms and running the stress testing. All other conditions, including flow rate and humidification were kept the same during the AST. The AST carried out was based on the DOE protocol for cathode-specific carbon corrosion [32], with cycling between 1 and 1.5 V at 500 mV s^{-1} for 5000 cycles. Cyclic voltammograms were collected after

0, 10, 100, 200, 1000, 2000 and 5000 cycles in order to follow the degradation of the electrochemical surface area (ECSA). ECSA was calculated following integration of the hydrogen desorption peak of the cyclic voltammogram, using the following equation:

$$ECSA = \frac{Q_{Hdes}}{\Gamma \cdot L} \qquad \text{Equation 3.1}$$

where Q_{Hdes} is the charge density of the hydrogen desorption peak in C cm^{-2}, Γ is the charge required to reduce a monolayer of hydrogen from the three crystal planes of platinum in C cm^{-2} (assumed here to be 210 C cm^{-2}) and L is the platinum loading in mg_{Pt} cm^{-2}, in this case 0.4 mg cm^{-2}.

After 0, 2000 and 5000 cycles, the cell was purged with nitrogen flow over the electrodes until the cell voltage was less than 0.1 V, then the sample was removed from the rig and imaging was carried out. The holder for mounting the sample onto the imaging stage was integrated into the cell by way of compression screws, for imaging of an identical location each time. Furthermore, image registration was used to align datasets after scanning, as will be discussed further in Section 3.2.

3.2 X-ray computed tomography

A scan of the whole fuel cell was done directly after cell assembly using a Nikon XT H 225 (Nikon, USA), to validate the alignment of the MEA with the flow channels, as well as to identify suitable regions of interest (ROIs) for further scanning at the micron length scale. Imaging was carried out using a source voltage of 145 kV and current of 106 µA. A total of 1786 radiographs were collected at a frame rate of one frame per second and following reconstruction using a filtered back-projection (FBP) reconstruction with the proprietary Nikon reconstruction software CT Pro 3D (Nikon, USA), the tomography dataset had a voxel size of 38 µm.

For X-ray micro-CT, a Zeiss XRadia Versa 520 (Zeiss, USA) was used. Samples were scanned at a beam voltage of 120 kV and beam power of 9 W. 1601 projections were collected with a 3 s exposure time using 4X optics, which, following reconstruction using a FBP algorithm, resulted in tomography datasets with a voxel size of 1.6 µm. For the three stages of cycling (0, 2000 and 5000 cycles), imaging was carried out on three locations across the flow-field, namely the cathode gas inlet, a central region

and the cathode gas outlet, with a total of nine separate scans being performed. In the resulting image dataset, features such as the land and channel, as well as the MEA, could be resolved (Figure 1b).

3.3 Transmission electron microscopy (TEM)

Transmission electron microscopy (TEM) was used to compare the platinum nanoparticle size distribution of a fresh electrode with the various regions of the degraded electrode. A Jeol JEM 2100 equipped with a LaB_6 source operated at 200 kV was used for imaging samples that were collected from the inlet, middle and outlet of the degraded cell (*i.e* after 5000 cycles). Samples were collected by lightly scraping the catalyst layer with a scalpel, taking care not to damage the MPL. This collected powder was dispersed by bath sonication in ethanol for 5 minutes before being drop-cast onto a TEM grid. In a similar manner a sample was also taken from a fresh GDE to provide a comparison. A total of 300 individual platinum nanoparticles were manually measured for each sample location and plotted as a histogram.

3.4 Image post-processing

Image post-processing was done primarily using Avizo Fire (Thermo Fisher Scientific, USA). Images were aligned using an image registration technique to account for any small movements of the sample that occurred during cycling. Datasets were first aligned as closely as possible by eye using manual registration, followed by automatic registration in Avizo using the Register Images module, which co-registers two closely aligned datasets using iterative optimisation algorithms. After image registration, an internal volume with dimensions 390 µm × 1720 µm × 2270 µm was extracted from all nine datasets, ensuring that for each imaging location (inlet, middle and outlet) the ROI was identical for the beginning-of-life (BOL), 2000 and 5000 cycle scan (Figure 1c). Datasets were segmented into four constituent phases (cathode CL, cathode cracks, anode CL and anode cracks) using local adaptive thresholding methods based on the grayscale histogram of each dataset (Figure 1d). After segmentation, local thickness of the cathode CLs were calculated using the "*LocalThickness*" plugin in ImageJ [33,34], with the results discussed in more detail in Section 4.3.

The extent of cracking was determined by taking the ratio of the crack volume fraction to the CL volume fraction, termed here the “cathode-crack ratio” (CCR) if pertaining to the cathode cracks, or “anode-crack ratio” (ACR) if pertaining to the anode cracks, according to the following:

$$CCR/ACR = \frac{V_{f(cracks)}}{V_{f(CL)} + V_{f(cracks)}} \times 100\% \qquad \text{Equation 3.2}$$

where $V_{f(cracks)}$ is the volume fraction of cracks in the electrode being investigated and $V_{f(CL)}$ is the volume fraction of the relevant catalyst layer. The volume fraction is defined as the percentage of the total volume of the dataset occupied by a particular phase, e.g. CL, MPL or fibres. Further investigations into extent of cracking included analysis of crack connectivity in the *yz*-plane. Using the “Axis Connectivity” module in Avizo, the extent of connectivity of cracks in the *z*- and *y*-planes were calculated, i.e. the extent to which cracks connect from one plane boundary to the opposite boundary. Percentage connectivity was then determined using Equations 3.3 and 3.4:

$$V_{f(connected)} = x_{connectivity} + y_{connectivity} \qquad \text{Equation 3.3}$$

$$\%\text{-}connectivity = \frac{V_{f(connected)}}{V_{f(cracks)}} \times 100\% \qquad \text{Equation 3.4}$$

where $x_{connectivity}$ and $y_{connectivity}$ are the volume fraction of connected cracks in the *x*- and *y*-axes, respectively, $V_{f(connected)}$ is the volume fraction of isolated regions that are connected between axes, $V_{f(cracks)}$ is the volume fraction of the cracks and %-connectivity is the percentage of connected cracks. Whilst the crack connectivity depends on the percolation of cracks across the entire length or width of a sample, it is a good indication for the extent of cracking in the CL of the various regions.

To further understand the internal connectivity of the cracks, points where the coordination number of nodes equal to three was calculated – a node value of three is considered to be a location where three cracks join together. Furthermore, label analysis was carried out on each dataset to understand the number of separately labelled cracks using the “*Label Analysis*” module in Avizo. This tool assigns a different “label” to each discreet, unconnected crack and this can be visualised by rendering the volumes of each crack. A greater number of labels represents a less well-connected crack network. Visualisation of the node and label analysis is found and discussed in more detail in Section 4.3.

For investigations where the location under land or channel was taken into account, a subvolume of dimensions 740 µm × 1700 µm × 580 µm was extracted (Figure 1b). Three different subvolumes were chosen for the land and channel of each location and results were averaged. Crack diameter was calculated using the "*LocalThickness*" plugin, as described before, and the average crack diameter was calculated for the land and channel regions in the samples. The CCR was also calculated for the three volumes in each region and the results were averaged. The land-channel analysis was done only for samples after 2000 and 5000 cycles, since all samples at BOL were fresh and, hence, there was no discernible difference between the crack diameter under the land and under the channel.

4 Results and discussion

4.1 Fuel cell performance

Polarisation curves taken after 0, 2000 and 5000 cycles showed a significant decrease in fuel cell performance over the course of the AST (Figure 2a), with the current density at 0.3 V falling from 300 mA cm^{-2} to 200 mA cm^{-2} to 37 mA cm^{-2} for BOL, 2000 and 5000 cycles, respectively (Figure 2a). Due to the operation of the cell at room temperature, there are high Ohmic over-potentials present. This highlights the need to introduce improved representability of technological systems in future work, which will include temperature control, as developed and demonstrated by White *et al.* [10,27]. After an initial steep drop of the ECSA, there was a less rapid decrease in the value after around 500 cycles (Figure 2b). Whilst the DOE protocol states a target of 40% loss of ECSA after 5000 cycles, the total percentage loss of ECSA was only 27%, falling from 54.8 $m^2 g_{Pt}^{-1}$ at BOL to 43.2 $m^2 g_{Pt}^{-1}$ after 2000 cycles to 40.2 $m^2 g_{Pt}^{-1}$ after 5000 cycles. This shows that whilst there has been a loss of active platinum surface area, the entire cell has not yet reached "failure". It is interesting to note that the drop in performance from 2000 cycles to 5000 cycles characterised by the polarisation curve is more significant than the change in the ECSA. This could indicate that after 5000 cycles the loss of platinum has slowed, whilst the carbon support has continued to degrade at some locations in the MEA, as will be discussed in Section 4.3. Although not observed in this work, the effect of continued carbon corrosion has been shown by Meyer *et al.* [35] and Castanheira *et al.* [6], where the presence of a

quinone/hydroquinone peak at 0.4 V – 0.7 V indicates an increase in C=O groups suggestive of increased carbon corrosion.

Furthermore, there has been an increase in the Ohmic losses at 2000 and 5000 cycles with the increasing loss of carbon support material, which could be due to a combination of increased contact resistance and reduced ease of proton conduction in the MEA. The contact resistances could arise due to increased cracking of the CL, which reduces the electrical connectivity of the CL to the GDL [10]. Water transport could be hindered as a result of the collapsing of the pore structure in the CL, which inhibits transport of ions through the CL, as suggested by Meyer *et al.* [35]. Several mechanisms for the degradation of carbon support as a result of the AST have been proposed in the literature, which relate to factors such as the humidity of the CL [9] and the type of cycling being done [13]. Finally, an additional "start-up/shut-down" effect is likely to have contributed to the degradation of the MEA, which arises when the AST is interrupted to carry out intermediate polarisation curves and imaging. The interruption will allow air to re-enter the cathode, as well as allow some drying of the MEA, and both of these factors have been shown to contribute to enhanced carbon-corrosion [36]. A further discussion of the mechanisms influencing the localised degradation in this study are given in Section 4.3.

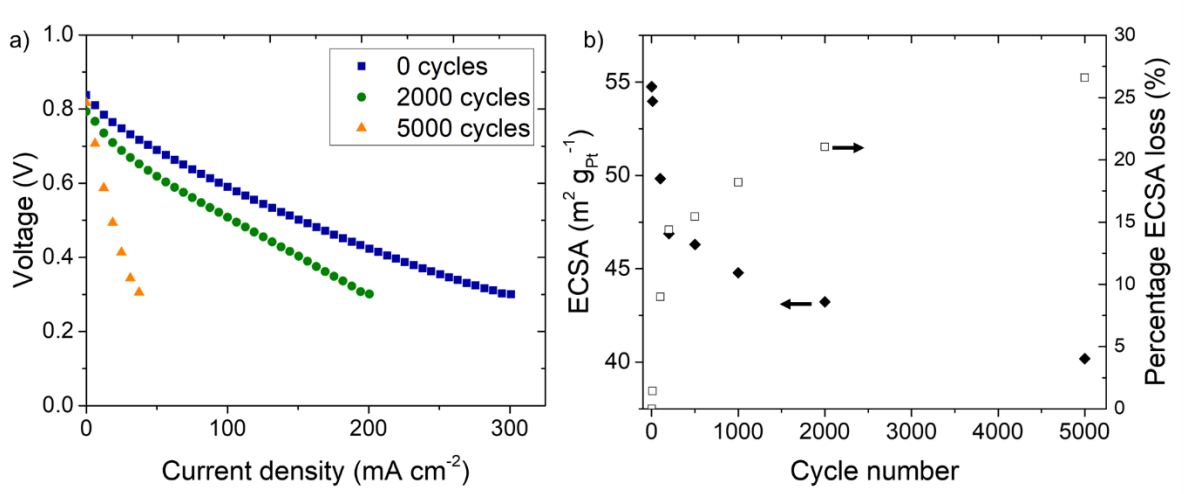

Figure 2 a) Polarisation curve and b) *in-situ* ECSA values calculated from the hydrogen adsorption peak of the cyclic voltammograms.

4.2 Imaging of regions

As was discussed in Section 3.2, a scan of the entire cell was carried out initially using the Nikon XT H 225 instrument (Figure 3a). Imaging of the whole cell showed that there was good alignment of components in the cell, with the MEA covering the entire flow-field. After scanning the whole cell, it was decided that the ROIs for microscale imaging would be the gas inlet on the cathode (with the cathode side determined by the orientation of the screws), a middle region across the fourth and fifth horizontal bends of the serpentine flow-field and the cathode gas outlet. A 1:1 ratio of channel:land was chosen for the serpentine design, based on modelling showing that a ratio equal to or greater than unity results in the most uniform current distribution [37].

The choice of 1 mm for the land and channel widths also ensured that both land and channel features would fit inside the field-of-view when carrying out the higher resolution scans. Even before segmentation, the various features of the MEA, land and channel can be distinguished according to the voxel grayscale value as can be seen for inlet, middle and outlet regions in Figure 3b-d, respectively. In this figure, the lighter regions correspond to the strongly attenuating CL and the land and channel regions are discernible by the darker grey colours, as indicated by the annotations.

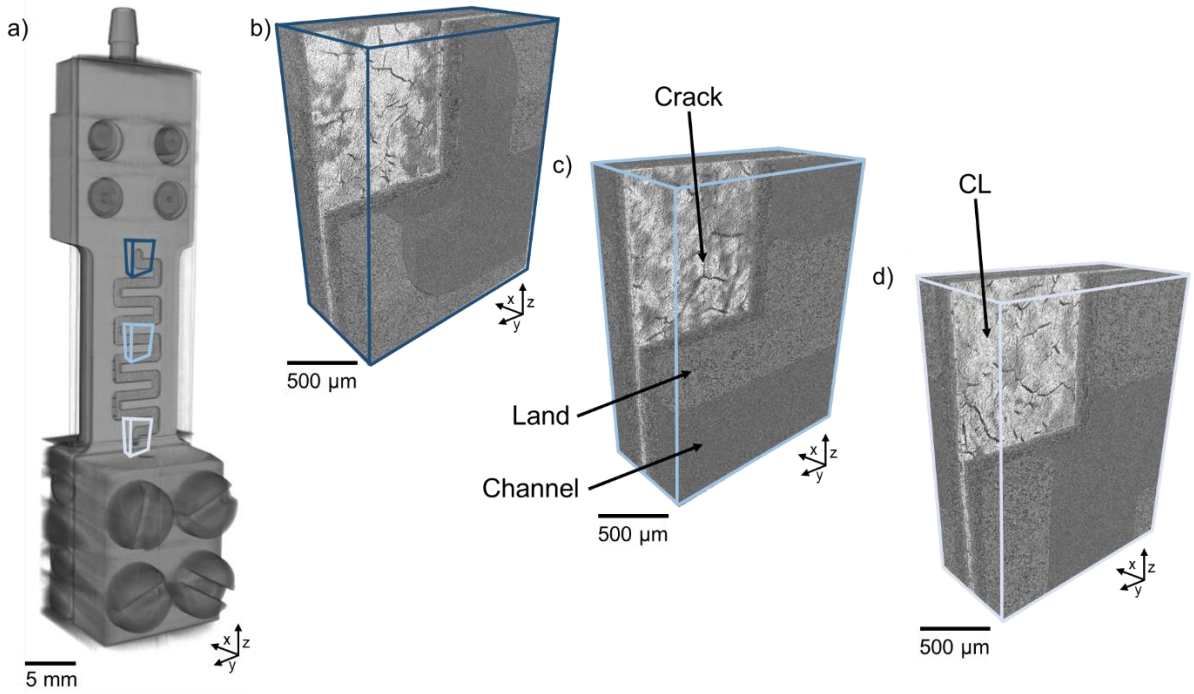

Figure 3 a) Macro-CT scan of the sample, showing the serpentine flow channels. The GDL is seen through the flow channel. The three ROIs have been indicated, with the colour of the bounding box corresponding to the ROI, as shown in the volumes imaged using X-ray micro-CT of the b) inlet, c) middle and d) outlet.

4.3 Localised cathode degradation

A total of nine scans were obtained, with three scans for each of the three ROIs at 0, 2000 and 5000 cycles and the cathode CL phase was visualised in the *yz* plane for each sample, where Figure 4a-c corresponds to the inlet, Figure 4d-f corresponds to the middle region and Figure 4g-i corresponds to the outlet. In each case, an outline of the flow-field location is indicated in the BOL sample using a black dotted line. Looking first at the effect of cycling on the morphology of the cathode CL, it can be seen that from 0 to 2000 to 5000 cycles (left-to-right in Figure 4), the extent of cracking increases with increasing cycling. Cracks that exist in the CL at BOL are found to act as nucleation points for crack growth over the course of cycling.

The CLs shown in Figure 4a-i are coloured according to the local thickness value indicated by the scale shown in the figure. It can be seen that some regions of the CL are slightly thicker, especially surrounding the cracks, as indicated by the red colour of the CL. It was also found that the local thickness across the CL tends to decrease with increasing cycling across the three regions of the MEA, an example which can be seen by the change of colour from red to yellow, as indicated by the arrow in Figure 4d, e and f. The average thickness of the CL was calculated from the local thickness histogram and results are shown in Table 1. It can be seen that for all three regions, the average CL thickness decreases, which highlights that as well as cracking, the CL is degrading by thinning of the catalyst layer, which has been shown to occur as a result of the collapse of the pore structure due to loss of carbon support [9]. This is also expected to have implications on the fuel cell performance, since a reduction in porosity of the CL would inhibit diffusion of gas and water through the CL, thus increasing mass transport losses [38]. It was found that the CL at the outlet had thinned to a greater extent than the middle and inlet CLs, with values of 18.0 μm, 15.7 μm and 14.7 μm for inlet, middle and outlet, respectively, after 5000 cycles. This provides a strong indication that the degradation is greater at the outlet than the inlet.

Table 1 Table showing the average CL thickness for each location at the various extent of cycling. Standard deviations, *σ*, are shown in brackets next to each value.

	CL thickness, inlet (*σ*) / µm	**CL thickness, middle (*σ*) / µm**	**CL thickness, outlet (*σ*) / µm**
0 cycles	21.1 (2.6)	21.6 (2.2)	22.0 (2.3)
2000 cycles	19.2 (2.2)	18.9 (2.0)	16.3 (2.0)
5000 cycles	18.0 (2.0)	15.7 (1.7)	14.7 (1.7)

Whilst the extent of cracking during cycling has been observed for different ASTs at a single location in the flow channel [10], to the authors' best knowledge, the along-the-channel degradation effects have been shown here using X-ray CT for the first time. Looking down the columns in Figure 4, it can be seen that at both 2000 and 5000 cycles, the extent of cracking and degradation of the CL is greater in the outlet than at the inlet, which is consistent with the findings of previous experiments using electrochemical current mapping techniques, such as the work done by Spernjak *et al.* [11]. This is particularly significant when considering the degradation of the MEA as a whole, as it indicates that many of the ASTs that are targeting catalyst or carbon support degradation are not degrading the MEA in a uniform manner. Furthermore, it highlights that whilst the electrochemical data provides an averaged performance across the entire MEA area, there could be regions of the cell that have failed, whilst others are still active. For example, the ECSA was found here to have decreased by 27%, but given the extent of degradation at the outlet, it could be the case that the outlet has already reached failure by 5000 cycles. The combination of current mapping with the *in-situ* X-ray CT imaging used in this work would be a valuable investigation to validate the localised performance of the CL and should be the subject of future work.

As discussed in Section 4.1, carbon corrosion arises as a function of the humidity of the system, as well as the effects of cycling at high voltages and it has been shown that lower overall humidity, or regions of lower humidity, experience greater degradation [39]. In addition, studies have shown that the presence of an air/hydrogen

mix (travelling wave) on the anode results in internal currents and elevated potentials that impact carbon corrosion [7,36,40]. Based on this knowledge, our hypothesis for the origins of the localised degradation are:

1. Near the inlet, the CL is well hydrated in this region due to the humidification of the inlet gases. Thus, carbon corrosion is mitigated due to the higher relative humidity and oxidation of water is occurring as the predominant reaction mechanism associated with the high potentials imposed by the AST.
2. Towards the central channels and outlet, as the MEA become less humidified due to consumption of the available water ‘upstream’ towards the entrance to the cell, the reaction mechanism shifts to favour carbon corrosion and greater breakdown of electrode material.

In order to verify the hypothesis here that the degradation rate is intrinsically linked to water content, validation of the water and humidity levels across the cell should be done with either neutron or X-ray CT imaging, or calculated using flow analysis, as the subject of future work. Furthermore, given the small size of this cell, comparative studies to larger systems would help to strengthen the hypotheses and observations discussed in this work.

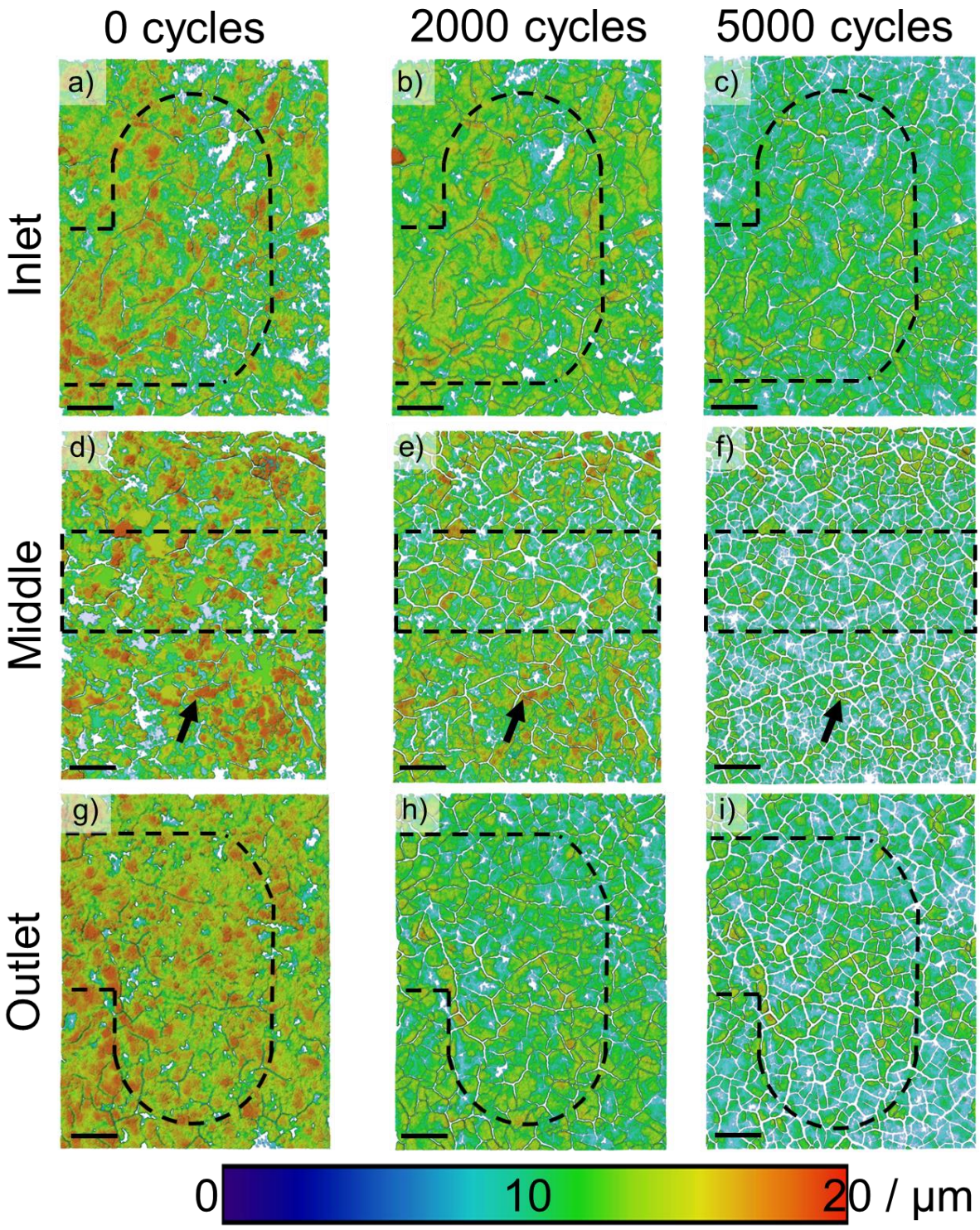

Figure 4 Cathode catalyst layer for a-c), inlet BOL, 2000 and 5000 cycles, respectively; d-f) middle BOL, 2000 and 5000 cycles, respectively; and g-i) outlet BOL, 2000 and 5000 cycles, respectively. Dashed line represents the outline of the flow field, with area outside being the land. Black scale bar represents 300 µm in each case. The colourbar indicated represents the local thickness of the CL, with increasing thickness of CL from green to red colour.

In order to quantify the different extent of degradation across regions of the MEA, Figure 5a shows the CCR that was calculated for the three regions according to Equation 3.2 at various stages of cycling. At BOL, the CCR for all three regions are similar, with only a 2% difference in the lowest (middle) and highest (outlet) CCR values. Even after 2000 cycles, it can be seen that the extent of cracking at the outlet has become the highest, with a value of 13%, compared with 10% and 7% for middle and inlet, respectively. This difference becomes yet more pronounced after 5000, with the outlet CCR value of 27% versus 18% in the middle region and 10% at the inlet. Overall, the inlet CCR was found to increase by 7%, whilst the middle region CCR increased by over double the amount (16%) and the outlet CCR value increased over three times the value of the inlet CCR, with an increase of 23%.

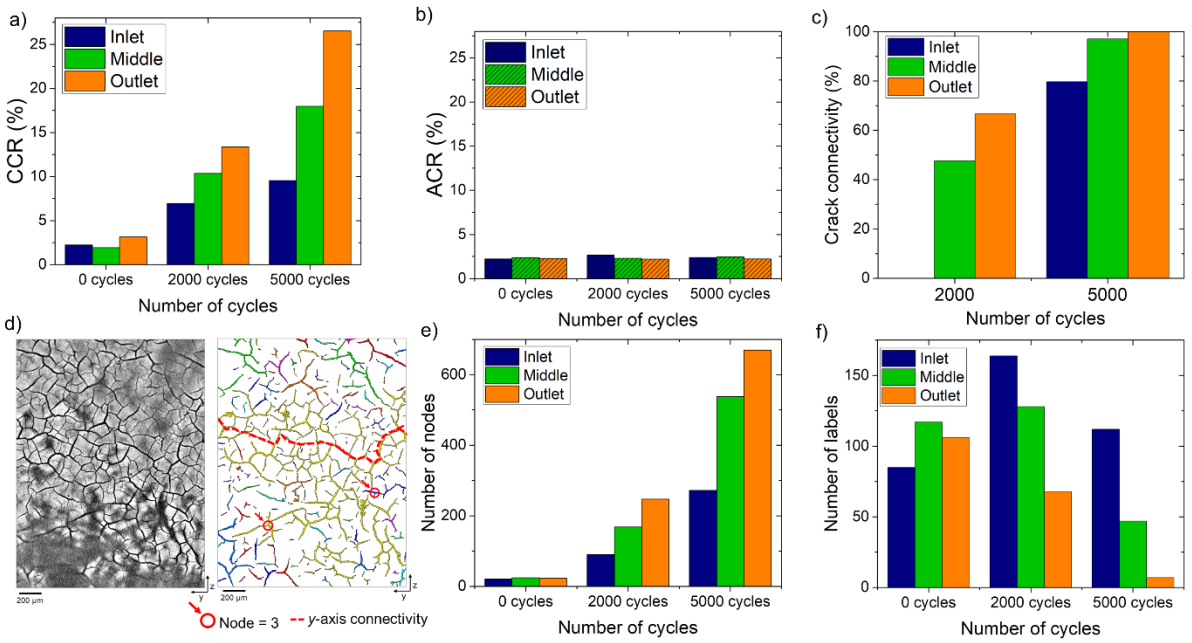

Figure 5 a) CCR and b) ACR for all stages of cycling for inlet (navy), middle (green) and outlet (orange); c) Crack connectivity shown for the inlet (navy), middle (green) and outlet (orange) regions; d) Grayscale orthoslice (left) and segmented crack network (right) of the middle region after 2000 cycles. Node regions and *y*-axis connectivity are indicated by a red circle and dashed line, respectively. Here only two examples of nodes and a single example of *y*-axis connectivity are indicated, but there are many more not indicated that are picked up by the analysis. In this image, each discreet isolated crack is represented by a label and these are assigned different colours. e) Graph showing the number of nodes where connectivity is equal to three and e) number of separate crack labels.

By way of comparison, ACR was calculated for the three regions at the stages of cycling and the results are shown in Figure 5b. It can be seen that for all three regions, the ACR is between 2.2% - 2.7% with no increase in cracking with over the course of cycling. This shows that the anode has not degraded as a result of the AST, which provides further evidence that the high extent of cracking on the cathode side is a direct result of electrochemical degradation.

Crack connectivity further highlighted the accelerated rate of degradation of the middle and outlet regions, compared with the inlet (Figure 5c). All three regions had 0% crack connectivity at BOL, with the only cracks present being a result of the drying of the CL ink during GDE manufacture. After 2000 cycles, the connectivity at the inlet was still found to be 0%, compared with 48% in the middle and the higher value of 67% at the outlet. This shows that the inlet has not yet degraded sufficiently to connect the cracks across the sample. At 5000 cycles, the inlet cracks have become connected in the *yz*-plane, with 80% of cracks connecting the axes. However, the connectivity is still between 17 and 20% lower than the connectivity of cracks in the middle and outlet, with 97% of cracks in the middle region being connected and 100% of the cracks in the outlet now connected. The increase in connectivity in all cases gives further evidence for a two-stage crack growth mechanism, whereby after 2000 cycles, existing cracks have grown and extended, with nucleation of new, unconnected cracks between these and after 5000 cycles, the smaller cracks have extended sufficiently to form a part of the connected crack network.

Analysis of the crack network provides further insight into the mechanisms for crack growth and propagation in the various regions over the course of cycling. This was done by analysing the crack connectivity in the *yz* plane and the number of nodes, with a few examples of these indicated on the segmented image of the cracks in Figure 5d. Analysis of the number of separate crack objects, as calculated by label analysis (Figure 5e), and number of nodes equal to 3 (Figure 5f) validates the trend observed in the other investigations. In all cases, the number of nodes increases with increasing cycling, with the number of nodes showing the level of crack branching and, hence, the extent of degradation. A greater number of nodes shows that there are more cracks that have branched from an existing crack. The number of nodes in the inlet after 5000 cycles is 272, which is 398 less than the number at the outlet and 266 less than in the

middle. This further highlights how the cracks in the middle and outlet are more connected than those at the inlet. The label analysis of the inlet and middle shows an increase in the number of separated cracks from 0 to 2000 cycles, followed by a decrease from 2000 to 5000 cycles. A larger number of labels suggests that there are more unconnected cracks in the network. Thus, while branching could increasingly be occurring, the new branches have not yet merged. The number of separated cracks in the outlet does not follow this trend and instead decreases with increasing cycle number. This could be attributed to the fact that the rate of degradation at the outlet is greater than in the middle or at the inlet and that significant degradation has already occurred by 2000 cycles. Thus, there are fewer separated cracks and instead, a more connected crack network exists. This phenomenon was also shown in the CCR and crack connectivity results, where the outlet displayed an accelerated crack formation compared with the other two regions.

Based on the findings here, the mechanism for crack growth is thought to be in line with previous reports [10,41–43], with crack propagation progressing *via* a two-step process of crack initiation followed by crack propagation, such as that shown in experimental/modelling work by Singh *et al.* [42]. Cracks that are present in the starting CL material (as characterised by the BOL scans) avoid the crack initiation step and degrade by way of widening and lengthening. Along these initial cracks, there are weaknesses and defects along the crack walls where the CL composition is irregular, as highlighted by Manahan *et al.* [43], which are thought to act as nucleation points for the initiation of new cracks and branches.

It is widely accepted that an effect of the carbon-support degradation test is the degradation of the platinum nanoparticles, by either agglomeration and particle growth, or loss of platinum altogether [44]. Thus, TEM studies were carried out and the results confirmed that there was degradation of the platinum nanoparticles as a result of carbon corrosion (Figure 6). TEM images in Figure 6 show examples of the sample extracted from each region, with the fresh electrode shown in Figure 6a, and the inlet, middle and outlet regions shown in Figure 6d, 6f and 6h, respectively. From the histogram of particles in the fresh electrode (Figure 6a), the maximum particle diameter was found to be 2.6 nm ± 0.4 nm. This is shifted to higher diameters for the degraded particles, with values of 3.4 ± 0.4 nm (Figure 6c), 3.7 ± 0.5 nm (Figure 6e)

and 3.5 ± 0.4 nm (Figure 6g) for inlet, middle and outlet, respectively. This increase in average particle size is in agreement with other work [45].

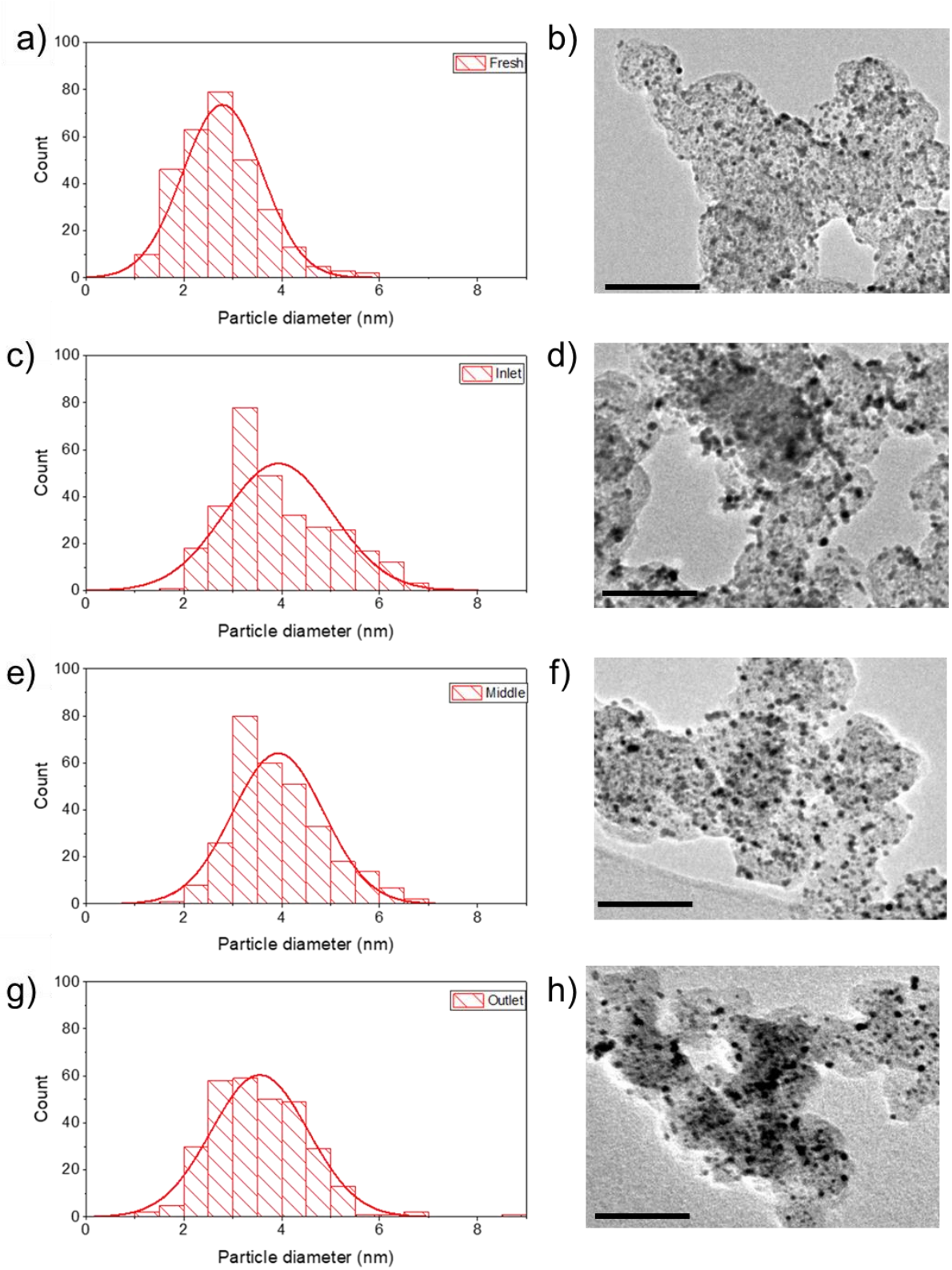

Figure 6 Histograms and TEM images of the particle diameter distributions for a a,b) fresh electrode and for the degraded electrodes at c,d) inlet, e,f) middle and g,h) outlet. Data was collected for 300 particles for each sample. Scalebar represents 50 nm in each image, (b,d,f,h).

4.4 Channel and land-specific degradation variations

In addition to the regional degradation of the MEA discussed in Section 4.3, there is also some variation in the extent of degradation of material that lies under a flow field channel or flow field land region. Previous studies have found that the extent of cracking under the channel is greater than under the land [10] and this is confirmed in the findings here. Looking at plots of the crack diameter under land regions and under channel regions (Figure 7a), it is possible to see by eye that the cracks in the channel region. This is especially noticeable in the middle and outlet regions, where the cracks are thicker than those in the land regions, as indicated by the shift from a purple to yellow colour, from thinner to thicker cracks.

The channel and land effect was investigated for the three regions after 2000 and 5000 cycles, by calculation of the average crack diameter (Figure 7b). It can be seen that the average crack diameter of the inlet for land and channel at 2000 cycles is very similar and even at 5000 cycles, there is only a 0.6 μm difference in the average crack width. On the other hand, the middle and outlet regions show that the channel crack width is, on average, larger than cracks falling under land regions, with a 1.7 μm difference after 2000 cycles and a 1.1 μm difference after 5000 cycles for the middle region. The outlet shows a similar trend with the channel region being 1.3 μm larger than the land region at 2000 cycles and 1.2 μm larger after 5000 cycles.

Calculation of the CCR for the land and channel region provides some further interesting insight into the properties of the cracks under the land and channel. Firstly, looking at the CCR after 2000 cycles (Figure 7c), it can be seen that the CCR_{land} is greater than $CCR_{channel}$ for both inlet and middle regions. In the case of the middle region, the cracks under the channel are on average thicker than the land, as was shown in Figure 7b, thus implying that there are fewer, thicker cracks that lie under the channel in the middle region. On the other hand, the outlet has the opposite trend, with the CCR_{land} less than the $CCR_{channel.}$ This suggests that the outlet region has already reached a “crack threshold”, where the volume of cracks under the channel has

exceeded a limit such that they are both wider and greater in number than under the land.

This “crack threshold” is observed further after 5000 cycles; whilst the CCR values for each land and channel region has increased as expected for inlet, middle and outlet, now the $CCR_{channel}$ is greater than CCR_{land} for both middle and outlet regions. This would suggest that the middle region has now reached the crack threshold, where the extent of cracking under the channel has become more significant than that under the land. Interestingly, the CCR for the inlet regions are almost the same, 15.0% ± 0.6 and 15.3% ± 1.7% for land and channel, respectively. This implies that the inlet region has approached, and indeed reached, the crack threshold after 5000 cycles.

Regarding the origins of the increased level of cracking under the channel than under the land, it is suggested that the degradation under the land is mitigated in two ways. Firstly, is has been shown by both modelling [46] and experimental [27] studies that water forms preferentially in regions under the land. Furthermore, this work has hypothesised that the greater humidity in the inlet region has the effect of reducing the rate of degradation. Thus, it is proposed that the higher volume of water under land regions has the effect of mitigating the degradation in regions under the land. As with the findings in previous sections, the validation by measurement of water across the MEA should be the subject of future work.

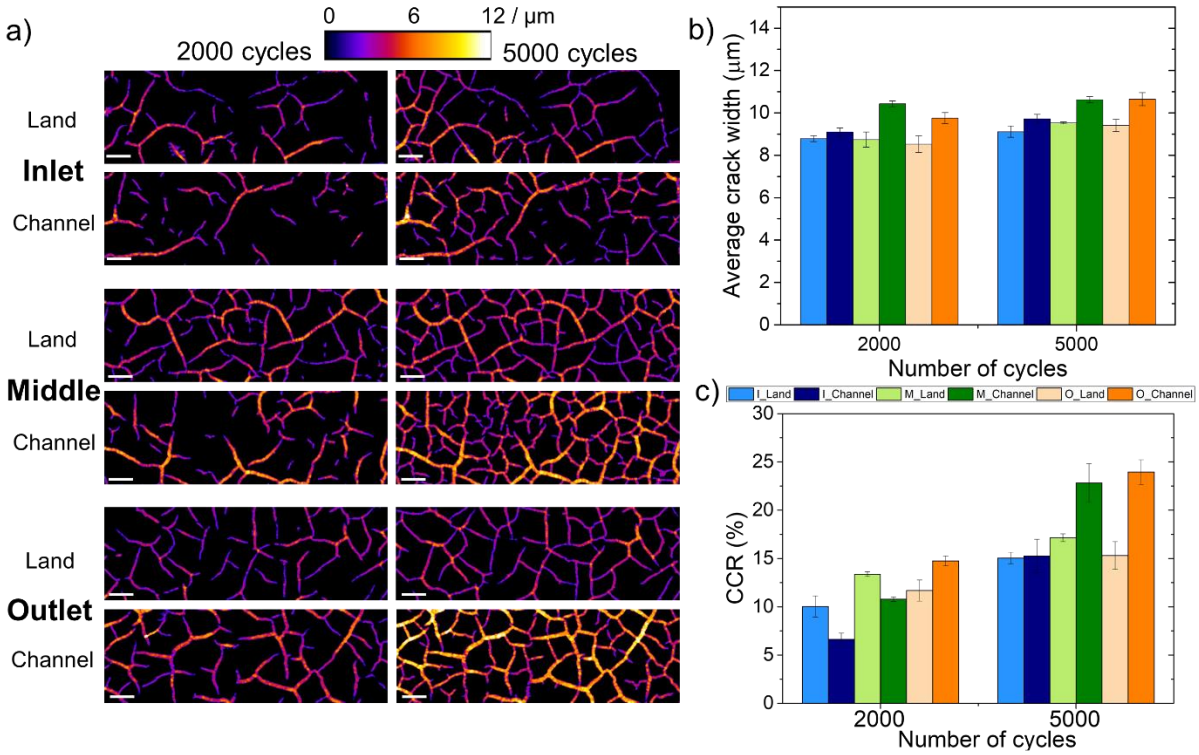

Figure 7 a) Images of the average crack width for inlet (top), middle (central) and outlet (bottom) regions. The colourmap corresponds to the crack width, with narrower cracks represented by purple/red colour and a yellow colour representing a thicker crack. Scalebars represent 100 µm; b) average crack widths and c) average CCR for each land and channel region. In b) and c), the inlet, middle and outlet regions are represented by blue, green and orange column colours, respectively, with lighter colours representing land regions and darker colours representing channel regions.

5 Conclusion

In this work, X-ray CT has been used for in-depth investigation of along-the-channel degradation of a cathode CL using a carbon corrosion specific AST. Identical-location X-ray micro-CT had been used to analyse the localised degradation of PEFCs across three regions of the flow-field during accelerated stress testing, namely the cathode gas inlet, a middle region and the cathode gas outlet. A bespoke cell was designed for testing, with a novel miniature design employing a serpentine flow-field design etched directly into the fuel cell end plate casing. Results of electrochemical testing showed a significant decrease in performance over the course of the AST, with a 27% loss of ECSA after 5000 cycles. To understand the mechanical degradation arising as a result of the AST, X-ray CT scans were performed after 0, 2000 and 5000 cycles of an AST at the three ROIs.

In all three regions, the cathode CL was found to degrade with increasing cycle number, primarily *via* formation and growth of crack networks. The anode did not degrade over the course of the AST. However, perhaps more significant was the observation that the rate of degradation across the three regions of the MEA varied significantly; the inlet was found to degrade less than the middle region, with the outlet region showing the largest amount of degradation. This was characterised by the development of a cathode-crack ratio (CCR) to quantify the extent of crack growth in the regions. Results showed that the CCR at 2000 and 5000 cycles was largest for the outlet, followed by the middle region and the inlet CCR being the smallest. Further quantification of the crack formation was done by analysis of the crack connectivity and label analysis. Results of these investigations highlighted further the localised nature of the degradation, with the outlet and middle regions being found to have a greater connection of the crack network in the CL than the inlet.

To investigate the degradation at the nanoparticle level, TEM studies were done on a fresh electrode and compared with samples extracted from the three regions. The average particle diameter of the fresh electrode platinum particles was found to be 2.6 nm ± 0.4 nm, with average diameters found to increase for the degraded electrode, ranging between 3.4 ± 0.4 nm at the inlet to 3.7 ± 0.5 nm in the middle, with the outlet falling between with a value of 3.5 nm ± 0.4.

Finally, analysis under the land and channel of the three regions was found to show that the extent of cracking under the land is less than under the channel, especially after 5000 cycles, characterised by the increased crack width under the channel, as well as a greater CCR under the channel is some cases.

The results shown here indicate that X-ray CT is a useful tool for quantifying the morphological degradation mechanisms along-the-channel of a serpentine flow field and confirm emerging findings that there is non-uniform localised performance across the MEA, from inlet to outlet. Furthermore, the results shown here indicate the need for intelligent MEA design, with graduated CL thickness or varying catalyst and carbon content from inlet to outlet being two suggested methods for balancing the degradation gradient across the MEA. Finally, investigations should be validated on larger operating cells, as well as including the quantification of water formation and probing

a wider range of AST protocols, given that the degradation of materials in the MEA is not limited to the carbon-corrosion-specific degradation investigated in this work.

6 Acknowledgements

Jennifer Hack would like to acknowledge a studentship from the EPSRC Centre for Doctoral Training in Advanced Characterisation of Material (EP/LO15277/1) and fuel cell research in the Electrochemical Innovation Lab through (EP/S018204/2, EP/R023581/1, EP/P009050/1, EP/L015749/1, EP/M014371/1, EP/M023508/1, EP/M009394/1, EP/L014289/1, EP/K038656/1). PLC would like to thank EPSRC for its continued support (EP/S001298/1).

7 References

[1] Z.P. Cano, D. Banham, S. Ye, A. Hintennach, J. Lu, M. Fowler, Z. Chen, Batteries and fuel cells for emerging electric vehicle markets, Nat. Energy. 3 (2018) 279–289. doi:10.1038/s41560-018-0108-1.

[2] Y. Wang, K.S. Chen, J. Mishler, S.C. Cho, X.C. Adroher, A review of polymer electrolyte membrane fuel cells: Technology, applications, and needs on fundamental research, Appl. Energy. 88 (2011) 981–1007. doi:http://dx.doi.org/10.1016/j.apenergy.2010.09.030.

[3] B.T. Sneed, D.A. Cullen, R. Mukundan, R.L. Borup, K.L. More, PtCo Cathode Catalyst Morphological and Compositional Changes after PEM Fuel Cell Accelerated Stress Testing, J. Electrochem. Soc. 165 (2018) F3078–F3084. doi:10.1149/2.0091806jes.

[4] J. Wu, X.Z. Yuan, J.J. Martin, H. Wang, J. Zhang, J. Shen, S. Wu, W. Merida, A review of PEM fuel cell durability: Degradation mechanisms and mitigation strategies, J. Power Sources. 184 (2008) 104–119. doi:10.1016/j.jpowsour.2008.06.006.

[5] R. Sharma, S.M. Andersen, An opinion on catalyst degradation mechanisms during catalyst support focused accelerated stress test (AST) for proton

exchange membrane fuel cells (PEMFCs), Appl. Catal. B Environ. 239 (2018) 636–643. doi:10.1016/j.apcatb.2018.08.045.

[6] L. Castanheira, W.O. Silva, F.H.B. Lima, A. Crisci, L. Dubau, F. Maillard, Carbon corrosion in proton-exchange membrane fuel cells: Effect of the carbon structure, the degradation protocol, and the gas atmosphere, ACS Catal. 5 (2015) 2184–2194. doi:10.1021/cs501973j.

[7] S. Kreitmeier, A. Wokaun, F.N. Büchi, Local Catalyst Support Degradation during Polymer Electrolyte Fuel Cell Start-Up and Shutdown, J. Electrochem. Soc. 159 (2012) F787–F793. doi:10.1149/2.019212jes.

[8] D. Seo, J. Lee, S. Park, J. Rhee, S.W. Choi, Y.-G. Shul, Investigation of MEA degradation in PEM fuel cell by on/off cyclic operation under different humid conditions, Int. J. Hydrogen Energy. 36 (2011) 1828–1836. doi:10.1016/J.IJHYDENE.2010.02.053.

[9] N. Macauley, D.D. Papadias, J. Fairweather, D. Spernjak, D. Langlois, R. Ahluwalia, K.L. More, R. Mukundan, R.L. Borup, Carbon Corrosion in PEM Fuel Cells and the Development of Accelerated Stress Tests, J. Electrochem. Soc. 165 (2018) F3148–F3160. doi:10.1149/2.0061806jes.

[10] R.T. White, A. Wu, M. Najm, F.P. Orfino, M. Dutta, E. Kjeang, 4D in situ visualization of electrode morphology changes during accelerated degradation in fuel cells by X-ray computed tomography, J. Power Sources. 350 (2017) 94–102. doi:10.1016/j.jpowsour.2017.03.058.

[11] D. Spernjak, J. Fairweather, R. Mukundan, T. Rockward, R.L. Borup, Influence of the microporous layer on carbon corrosion in the catalyst layer of a polymer electrolyte membrane fuel cell, J. Power Sources. 214 (2012) 386–398. doi:10.1016/J.JPOWSOUR.2012.04.086.

[12] Y. Singh, R.T. White, M. Najm, T. Haddow, V. Pan, F.P. Orfino, M. Dutta, E. Kjeang, Tracking the evolution of mechanical degradation in fuel cell membranes using 4D in situ visualization, J. Power Sources. 412 (2019) 224–237. doi:10.1016/j.jpowsour.2018.11.049.

[13] J. Speder, A. Zana, I. Spanos, J.J.K. Kirkensgaard, K. Mortensen, M. Hanzlik,

M. Arenz, Comparative degradation study of carbon supported proton exchange membrane fuel cell electrocatalysts - The influence of the platinum to carbon ratio on the degradation rate, J. Power Sources. 261 (2014) 14–22. doi:10.1016/j.jpowsour.2014.03.039.

[14] Q. Meyer, Y. Zeng, C. Zhao, In Situ and Operando Characterization of Proton Exchange Membrane Fuel Cells, Adv. Mater. 31 (2019) 1901900. doi:10.1002/adma.201901900.

[15] T.M.M. Heenan, C. Tan, J. Hack, D.J.L. Brett, P.R. Shearing, Developments in X-ray tomography characterization for electrochemical devices, Mater. Today. 31 (2019) 69–85. doi:10.1016/j.mattod.2019.05.019.

[16] J. Eller, J. Roth, F. Marone, M. Stampanoni, F.N. Büchi, Operando Properties of Gas Diffusion Layers: Saturation and Liquid Permeability, J. Electrochem. Soc. 164 (2017) F115–F126. doi:10.1149/2.0881702jes.

[17] I. V. Zenyuk, Bridging X-ray computed tomography and computational modeling for electrochemical energy-conversion and –storage, Curr. Opin. Electrochem. 13 (2019) 78–85. doi:10.1016/j.coelec.2018.10.016.

[18] S. Chevalier, J. Lee, N. Ge, R. Yip, P. Antonacci, Y. Tabuchi, T. Kotaka, A. Bazylak, In operando measurements of liquid water saturation distributions and effective diffusivities of polymer electrolyte membrane fuel cell gas diffusion layers, Electrochim. Acta. 210 (2016) 792–803. doi:10.1016/j.electacta.2016.05.180.

[19] R.T. White, F.P. Orfino, M. El Hannach, O. Luo, M. Dutta, A.P. Young, E. Kjeang, 3D Printed Flow Field and Fixture for Visualization of Water Distribution in Fuel Cells by X-ray Computed Tomography, J. Electrochem. Soc. 163 (2016) F1337–F1343. doi:10.1149/2.0461613jes.

[20] J. Eller, F.N. Büchi, Polymer electrolyte fuel cell performance degradation at different synchrotron beam intensities, J. Synchrotron Radiat. 21 (2014) 82–88. doi:10.1107/S1600577513025162.

[21] R.T. White, M. Najm, M. Dutta, F.P. Orfino, E. Kjeang, Communication—Effect of Micro-XCT X-ray Exposure on the Performance of Polymer Electrolyte Fuel

Cells, J. Electrochem. Soc. 163 (2016) F1206–F1208. doi:10.1149/2.0751610jes.

[22] S.S. Alrwashdeh, I. Manke, H. Markötter, M. Klages, M. Göbel, J. Haußmann, J. Scholta, J. Banhart, In Operando Quantification of Three-Dimensional Water Distribution in Nanoporous Carbon-Based Layers in Polymer Electrolyte Membrane Fuel Cells, ACS Nano. 11 (2017) 5944–5949. doi:10.1021/acsnano.7b01720.

[23] S.J. Normile, D.C. Sabarirajan, O. Calzada, V. De Andrade, X. Xiao, P. Mandal, D.Y. Parkinson, A. Serov, P. Atanassov, I. V. Zenyuk, Direct observations of liquid water formation at nano- and micro-scale in platinum group metal-free electrodes by operando X-ray computed tomography, Mater. Today Energy. 9 (2018) 187–197. doi:10.1016/j.mtener.2018.05.011.

[24] J. Eller, F. Marone, F.N. Büchi, Operando sub-second tomographic imaging of water in PEFC gas diffusion layers, ECS Trans. 69 (2015) 523–531. doi:10.1149/06917.0523ecst.

[25] D. Ramani, Y. Singh, F.P. Orfino, M. Dutta, E. Kjeang, Characterization of Membrane Degradation Growth in Fuel Cells Using X-ray Computed Tomography, J. Electrochem. Soc. 165 (2018) F3200–F3208. doi:10.1149/2.0251806jes.

[26] Y. Singh, F.P. Orfino, M. Dutta, E. Kjeang, 3D visualization of membrane failures in fuel cells, J. Power Sources. 345 (2017) 1–11. doi:10.1016/j.jpowsour.2017.01.129.

[27] R.T. White, S.H. Eberhardt, Y. Singh, T. Haddow, M. Dutta, F.P. Orfino, E. Kjeang, Four-dimensional joint visualization of electrode degradation and liquid water distribution inside operating polymer electrolyte fuel cells, Sci. Rep. 9 (2019) 1–12. doi:10.1038/s41598-018-38464-9.

[28] S. Komini Babu, D. Spernjak, J. Dillet, A. Lamibrac, G. Maranzana, S. Didierjean, O. Lottin, R.L. Borup, R. Mukundan, Spatially resolved degradation during startup and shutdown in polymer electrolyte membrane fuel cell operation, Appl. Energy. 254 (2019) 113659.

doi:10.1016/j.apenergy.2019.113659.

[29] D. Garcia-Sanchez, T. Morawietz, P.G. da Rocha, R. Hiesgen, P. Gazdzicki, K.A. Friedrich, Local impact of load cycling on degradation in polymer electrolyte fuel cells, Appl. Energy. 259 (2020). doi:10.1016/j.apenergy.2019.114210.

[30] S. Ghosh, H. Ohashi, H. Tabata, Y. Hashimasa, T. Yamaguchi, In-plane and through-plane non-uniform carbon corrosion of polymer electrolyte fuel cell cathode catalyst layer during extended potential cycles, J. Power Sources. 362 (2017) 291–298. doi:10.1016/j.jpowsour.2017.07.017.

[31] S. Takao, O. Sekizawa, G. Samjeské, S. ichi Nagamatsu, T. Kaneko, K. Higashi, T. Yamamoto, K. Nagasawa, X. Zhao, T. Uruga, Y. Iwasawa, Spatially Non-Uniform Degradation of Pt/C Cathode Catalysts in Polymer Electrolyte Fuel Cells Imaged by Combination of Nano XAFS and STEM-EDS Techniques, Top. Catal. 59 (2016) 1722–1731. doi:10.1007/s11244-016-0691-y.

[32] U.S. DRIVE Fuel Cell Tech Team, Fuel Cell Tech Team AST and Polarization Curve Protocols for PEMFCs, U.S. DRIVE Fuel Cell Tech Team. (2013). https://energy.gov/sites/prod/files/2015/08/f25/fcto_dwg_usdrive_fctt_accelerated_stress_tests_jan2013.pdf (accessed December 6, 2017).

[33] R. Dougherty, K.-H. Kunzelmann, Computing Local Thickness of 3D Structures with ImageJ, Microsc. Microanal. 13 (2007) 1678–1679. doi:10.1017/s1431927607074430.

[34] C.A. Schneider, W.S. Rasband, K.W. Eliceiri, NIH Image to ImageJ: 25 years of image analysis, Nat. Methods. 9 (2012) 671–675. doi:10.1038/nmeth.2089.

[35] Q. Meyer, Y. Zeng, C. Zhao, Electrochemical impedance spectroscopy of catalyst and carbon degradations in proton exchange membrane fuel cells, J. Power Sources. 437 (2019) 226922. doi:10.1016/J.JPOWSOUR.2019.226922.

[36] F.A. De Bruijn, V.A.T. Dam, G.J.M. Janssen, Review: Durability and degradation issues of PEM fuel cell components, Fuel Cells. 8 (2008) 3–22. doi:10.1002/fuce.200700053.

[37] H. Kahraman, M.F. Orhan, Flow field bipolar plates in a proton exchange membrane fuel cell: Analysis & modeling, Energy Convers. Manag. 133 (2017) 363–384. doi:10.1016/j.enconman.2016.10.053.

[38] A. Pokhrel, M. El Hannach, F.P. Orfino, M. Dutta, E. Kjeang, Failure analysis of fuel cell electrodes using three-dimensional multi-length scale X-ray computed tomography, J. Power Sources. 329 (2016) 330–338. doi:http://dx.doi.org/10.1016/j.jpowsour.2016.08.092.

[39] R.L. Borup, J.R. Davey, F.H. Garzon, D.L. Wood, M.A. Inbody, PEM fuel cell electrocatalyst durability measurements, J. Power Sources. 163 (2006) 76–81. doi:10.1016/j.jpowsour.2006.03.009.

[40] C. Lee, W. Mérida, Gas diffusion layer durability under steady-state and freezing conditions, J. Power Sources. 164 (2007) 141–153. doi:10.1016/j.jpowsour.2006.09.092.

[41] Y. Chang, J. Liu, R. Li, J. Zhao, Y. Qin, J. Zhang, Y. Yin, X. Li, Effect of humidity and thermal cycling on the catalyst layer structural changes in polymer electrolyte membrane fuel cells, Energy Convers. Manag. 189 (2019) 24–32. doi:10.1016/J.ENCONMAN.2019.03.066.

[42] Y. Singh, R.M.H. Khorasany, W.H.J. Kim, A.S. Alavijeh, E. Kjeang, R.K.N.D. Rajapakse, G.G. Wang, Ex situ characterization and modelling of fatigue crack propagation in catalyst coated membrane composites for fuel cell applications, Int. J. Hydrogen Energy. 44 (2019) 12057–12072. doi:10.1016/J.IJHYDENE.2019.03.108.

[43] M.P. Manahan, S. Kim, E.C. Kumbur, M.M. Mench, Effects of Surface Irregularities and Interfacial Cracks on Polymer Electrolyte Fuel Cell Performance, ECS Trans. 25 (2009) 1745–1754. doi:10.1149/1.3210730.

[44] S. Takao, O. Sekizawa, G. Samjeské, T. Kaneko, K. Higashi, Y. Yoshida, X. Zhao, T. Sakata, T. Yamamoto, T. Gunji, T. Uruga, Y. Iwasawa, Observation of Degradation of Pt and Carbon Support in Polymer Electrolyte Fuel Cell Using Combined Nano-X-ray Absorption Fine Structure and Transmission Electron Microscopy Techniques, ACS Appl. Mater. Interfaces. 10 (2018) 27734–

27744. doi:10.1021/acsami.8b04407.

[45] R. Sharma, S. Gyergyek, Q. Li, S.M. Andersen, Evolution of the degradation mechanisms with the number of stress cycles during an accelerated stress test of carbon supported platinum nanoparticles, J. Electroanal. Chem. 838 (2019) 82–88. doi:10.1016/j.jelechem.2019.02.052.

[46] C. Wang, Q. Zhang, S. Shen, X. Yan, F. Zhu, X. Cheng, J. Zhang, The respective effect of under-rib convection and pressure drop of flow fields on the performance of PEM fuel cells, Sci. Rep. 7 (2017) 1–9. doi:10.1038/srep43447.